*Mineralogical Magazine, October 2003, Vol. 67(5), pp. 1059–1080*

# Iron sulphides at the epithermal gold-copper deposit of Palai-Islica (Almería, SE Spain)

F. J. Carrillo Rosúa, S. Morales Ruano* and P. Fenoll Hach-Alí

Department of Mineralogy and Petrology, University of Granada and Instituto Andaluz de Ciencias de la Tierra (CSIC-UGR), Avda. Fuentenueva s/n. E-18002, Granada, Spain

**ABSTRACT**

Au-Cu mineralization at Palai-Islica occurs as disseminations in massive silicified volcanic rocks and, more abundantly, in sulphide-bearing quartz veins. The major ore minerals in the deposit are pyrite ± chalcopyrite, sphalerite and galena and there is a great variety of accessory minerals, including Au-Ag alloys and native gold. Pyrite, the most abundant sulphide, is closely associated with gold. Seven different types of pyrite have been distinguished with a variable concentration of different trace elements. Among these, the only one free of trace elements (type IV) is related to Au-Ag alloys. Pyrite associated with these Au-Ag alloys has cubic and pentagonal dodecahedral habits, whereas pyrite with pentagonal dodecahedral habit only is from barren zones. In addition, there is no significant invisible gold in the pyrite, but there is a relatively large amount of Ag in collomorphic pyrite (up to 0.20 wt.%) or type III pyrite (up to 1.47 wt.%). Arsenic is the most abundant trace element in pyrite (up to 6.11 wt.%), present as a metastable solid solution or as a non-stoichiometric element. A variety of marcasite related to the gold levels also has a considerable amount of trace elements (As up to 1.15 wt.%, Sb up to 0.40 wt.%).

**Keywords:** pyrite, gold, epithermal deposit, Spain.

## Introduction

Pyrite is the most common sulphide in the Earth's crust and it forms under a wide range of conditions (Craig *et al*., 1998), e.g. in sedimentary, metamorphic, igneous and hydrothermal environments. It reaches its greatest abundance and is the most common mineral in hydrothermal environments (Ramdohr, 1980). It displays significant textural and morphological diversity (Murowchick and Barnes, 1987) and its chemical composition can also vary considerably, particularly with respect to Co, Ni and As (Rösler, 1983). The Co and Ni can enter into its crystalline structure, forming a solid solution with vaesite and catierite (Kostov and Minceva-Stefanova, 1981). Although As occurs in equilibrium in minor amounts (up to 0.5 wt.%) in synthetic pyrite (Clark, 1960), natural pyrite may contain as much as 9.44 wt.% As (Ashley *et al*., 2000). More important is the fact that pyrite is a collector of precious metals, such as Au and Ag (Boyle, 1979; Roberts, 1982) as well as platinum group elements (Rypley and Chryssoulis, 1994). Therefore, its chemistry has been investigated in many deposits using diverse analytical techniques (e.g. Griffin *et al*., 1991; Arehart *et al*., 1993; Morales Ruano, 1994; Rypley and Chryssoulis, 1994; Huston *et al*., 1995; Ashley *et al*., 2000). Study of pyrite chemistry may also be useful in foreseeing, planning and, if needed, minimizing the environmental impact that can be caused by heavy-element contaminants produced by leaching of mine tailings.

In the Cu-Au deposit at Palai-Islica, pyrite is the main Fe sulphide, where it is closely associated with gold (Carrillo Rosúa *et al*., 2001*b*, 2002). The present work aims to establish

* E-mail: smorales@ugr.es
DOI: 10.1180/0026461036750143

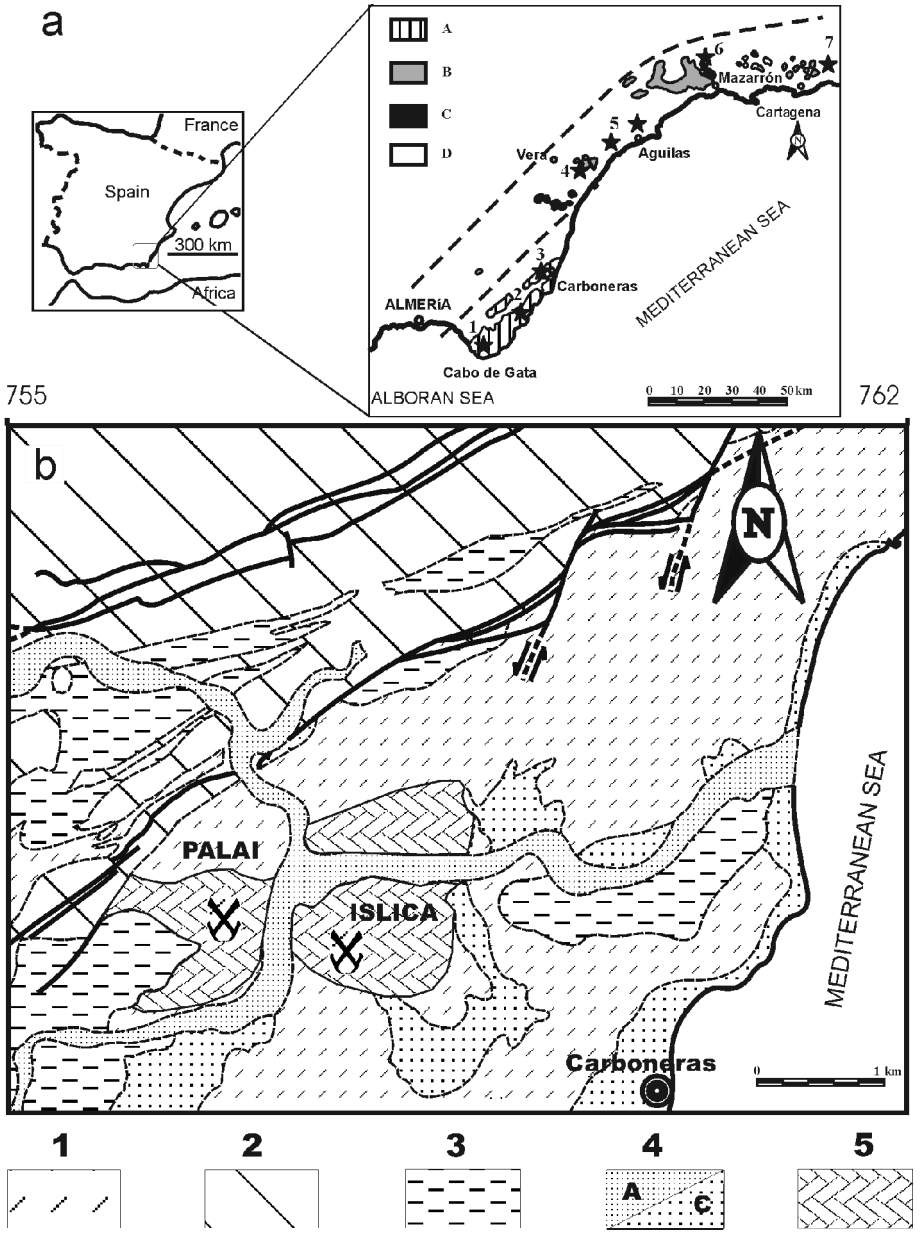


FIG. 1. (*a*) Location of the main groups of volcanic rocks in the Cabo de Gata-Cartagena volcanic belt (adapted from Lopez Ruiz and Rodriguez Badiola, 1980): (A) calc-alkaline volcanism; (B) calc-alkaline, potassic and shoshonitic volcanism; (C) ultrapotassic volcanism; (D) basaltic volcanism. The most important ore deposits are: (1) Cabo de Gata; (2) Rodalquilar; (3) Carboneras (Palai-Islica); (4) Herrerías and Sierra Almagrera; (5) Aguilas; (6) Mazarrón; (7) Cartagena. (*b*) Schematic geological map showing the location of the Palai-Islica deposit (adapted from IGME, 1974). Main geological units: (1) Upper Miocene volcanic rocks of the Cabo de Gata calco-alkaline series; (2) Palaeozoic-Mesozoic basement rocks belonging to the Alpujarride and Malaguide Complexes; (3) Tertiary sedimentary rocks; (4) Quaternary sediments (a) alluvial and (c) colluvial; (5) Outcropping Palai-Islica mineralization and zone of hydrothermal alteration. Faults are indicated by solid black lines. (Figure slightly modified from Morales *et al*., 2000)

possible mineralogical, textural and chemical affinities between gold and the distinct varieties of pyrite. We focus on the textural and mineral chemistry characteristics of pyrite and other associated Fe sulphides (pyrrhotite and marcasite) and their crystallochemical and geochemical implications. Pyrite also contains potentially significant amounts of trace element contaminants which are an important factor since the Palai-Islica deposit is located in the vicinity of the Cabo de Gata Natural Park.

## Geological context

The main geological features of the area of the Palai-Islica deposit are well known (Arribas and Tosdal, 1994; Fernandez Sóler, 1996; Turner *et al.*, 1999), and only a summary is given here (see also Morales Ruano *et al.*, 2000). The Palai-Islica deposit lies within the volcanic belt of Cabo de Gata-Cartagena (Fig. 1*a*), which comprises part of the eastern end of the Internal Zone of the Betic Cordilleras. This Neogene volcanic belt, with different series of volcanic rocks (calc-alkaline, shoshonitic, potassic calc-alkaline, ultrapotassic and basaltic series (López Ruiz and Rodriguez Badiola, 1980)), formed within the context of a subduction zone, followed by an extensional event (Dewey, 1988; García Dueñas *et al.*, 1992). During the Miocene, a series of magmatism-related hydrothermal systems developed, being controlled by a system of faults and fractures. The hot fluids (up to 400–450ºC, Morales Ruano (1994)) reacted strongly with the host rocks and, in some districts, gave rise to broad areas of mineralization and alteration (Fig. 1*a*), usually zoned (Fernández Soler, 1996) as in the Rodalquilar deposit where propylitic, argillic, advanced argillic and silicic alteration have been observed from the outer to inner zones (Arribas *et al.*, 1995). The Palai-Islica is one of these areas which has become a recent target of mineral exploration companies (Morales Ruano *et al.*, 2000). The Cu-Au epithermal mineralization of Palai-Islica (Fig. 1*b*) is hosted by hydrothermally alterated calc-alkaline volcanic rocks (mainly dacites and andesites of Miocene age) related to regional strike-slip faults (N40–50E) (Fernandez Soler, 1996). The alteration area (propylitic, sericitic, argillic, silicification) consists of an oval, E–W-striking zone, 2500 m long by 1700 m wide, to which the gold mineralization is invariably related (Morales Ruano *et al.*, 2000).

## Sampling and methodology

Samples were obtained from various areas of high-grade gold and barren mineralization at Palai-Islica. Two hundred and twenty-two polished thin-sections of samples collected from 21 drill cores were prepared to determine the mineralogy and the paragenetic relationships in this deposit.

The mineralogical, chemical and textural characteristics of Fe sulphides were determined by reflected and transmitted light microscopy, scanning electron microscopy, SEM (ZEISS DSM 950) and FESEM (LEO GEMINI) and electron microprobe, EPMA (CAMECA SX50) at the Centro de Instrumentación Científica of the University of Granada. Scanning electron microscopy (SEM) was used to detect As-rich zones, followed by better-quality, backscattered images using electron probe microanalysis (EPMA) on chosen fields. X-ray mapping, with EPMA identified zonings of other elements (e.g. Co and Ni) that are not easily detectable by SEM. The operating conditions for the X-ray mapping were 30 kV accelerating potential, 200 nA beam current, 2 μm scan distance, and 300 ms X-ray peak acquisition time per point. The information obtained by electronic images, qualitative EPMA profiles, was used to perform the analysis of Fe sulphides in selected points of representative areas. A total of 399 analysis were obtained by EPMA.

Natural and synthetic-certified standards were used to calibrate the quantitative analysis. The operating conditions were 30 kV accelerating potential, 30 nA beam current and acquisition time between 60 and 300 s for X-ray peak and background. Fifteen selected analyses of Au with a lower detection limit (475 ppm, 95% confident) were performed for pyrite (100 nA bean current with acquisition times of 2000 s for X-ray peak and background). The acquired X-ray intensities were corrected for atomic number, mass absorption and secondary fluorescence effects using the CAMECA-PAP version of the Pouchou and Pichoir (1984) procedure.

## Ore mineralization

The mineralization at Palai-Islica is: (1) disseminated in massively silicified volcanic rocks, located exclusively in the highest part of the deposit; (2) disseminated within the ubiquitously hydrothermally altered rocks; and (3) most abundantly, in sulphide-bearing quartz veins.

The occurrences in veins have been described by Morales Ruano *et al.* (2000) and Carrillo Rosúa *et al.* (2001*a*) for three subhorizontal levels. They are characterized by Au-Ag alloys, greater mineralogical diversity, enrichment in Au, Ag, Zn, Pb, Cd, As and Sb and fluids with distinct characteristics (wide variation in salinity over a narrow temperature range) relative to the rest of the deposit.

The ore minerals in the deposit (Morales Ruano *et al.*, 1999; Carrillo Rosúa *et al.*, 2001*a*) consist primarily of pyrite with occasionally large chalcopyrite, sphalerite and galena contents. There is also a number of accessory minerals, such as gold, tetrahedrite-tennantite, bismuthinite, Ag±Bi±Pb±(Cu) sulphosalts, Ag and Bi tellurides, Ag sulphides and sulphosalts (achantite, polybasite-pearcite, proustite-pyrargyrite, stephanite), pyrrhotite, marcasite, Cu sulphides (bornite, chalcocite, covellite), stannite, niccolite, arsenopyrite, native copper and Fe-Ti-Sn oxides (rutile, magnetite, hematite, cassiterite).

According to Carrillo Rosúa *et al.* (2001*a*, 2002), the gold occurs as native gold (disseminated exclusively in the massive silicifications) and as Au-Ag alloys in the sulphide-bearing quartz veins. These alloys are relatively abundant, and are always closely associated with pyrite, either included within it (Au-rich alloys) or as overgrowths (Ag-rich alloys) (Fig. 2).

## Mineralogical, textural and chemical characteristics of the Fe sulphides

Fe sulphides, and in particular pyrite, are by far the most abundant sulphides in this deposit, displaying a great variety of textural and chemical types. There are three varieties of Fe sulphides.

(1) Pyrrhotite (diameter <100 μm) appears included within porous pyrite, sometimes intergrown with chalcopyrite or magnetite. Chemical analysis of pyrrhotite gave the formula $Fe_{0.84-0.91}S$, with very low concentrations of trace elements (Table 1).

(2) Marcasite also occurs in minor amounts filling late microveins, disseminated crystals in the massive silcification, disseminated in the volcanic rock of the deepest zones of the deposit, intergrown with pyrite in micro-geodes or as idiomorphic crystals in a peculiar association with pyrite and chalcopyrite as follows (Fig. 3*a*): (a) pyrite cores sometimes with tiny inclusions of a Ag-bearing phases; (b) not always present, elongated chalcopyrite crystals following the limit between pyrite and marcasite; (c) idiomorphic marcasite crystals. (d) collomorphic pyrite overgrown on marcasite. This mineral association is located at the top of Au-Ag alloy bearing levels. Marcasite does not show chemical zonation as it is quite pure (Table 1) with the exception of the last textural case (Fig. 3*b*). This has significant quantities of As (up to 1.15 wt.%) and Sb (up to 0.40 wt.%) concentrated in irregular zones in marcasite (Fig. 3*c,d*), corresponding to the maximum concentration of Sb with the intermediate of As (Fig. 4*a*). The increase of As is accompanied by a decrease in the sulphur concentration of the same order (Fig. 4*b*). In contrast with associated pyrite, marcasite has small Cu and Ag contents (Fig. 3*f,g*).

(3) Pyrite is by far the most abundant phase. Two groups of pyrite are recognized, based on

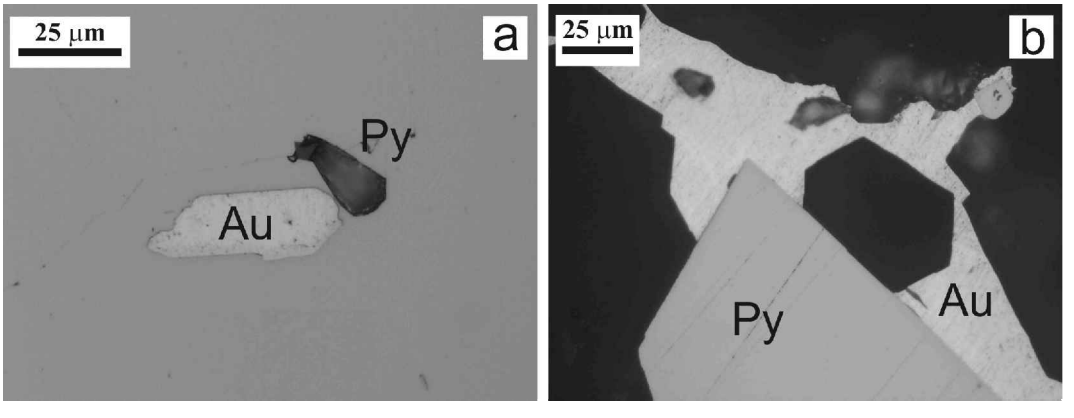


FIG. 2. Photomicrographs of Au-Ag alloy: (*a*) Crystal of homogeneous Au-Ag alloy (Au) included in a non-porous type IV pyrite (Py). (*b*) Crystal of Au-Ag alloy (Au) overgrowing type IV pyrite (Py).

TABLE 1. Chemistry of pyrrhotite and marcasite.

| | A ($n$ = 8) | | | | B ($n$ = 31) | | | | C ($n$ = 3) | | | |
|---|---|---|---|---|---|---|---|---|---|---|---|---|
| Wt.% | Min | Max | Ave | s.d. (1σ) | Min | Max | Ave | s.d. (1σ) | Min | Max | Ave | s.d. (1σ) |
| Au | 0.00 | 0.06 | 0.03 | 0.02 | 0.00 | 0.05 | 0.02 | 0.02 | 0.02 | 0.04 | 0.03 | 0.01 |
| Ag | 0.00 | 0.03 | 0.02 | 0.01 | 0.00 | 0.05 | 0.02 | 0.01 | 0.00 | 0.02 | 0.01 | 0.01 |
| S | 37.87 | 39.93 | 38.64 | 0.65 | 51.63 | 53.81 | 52.92 | 0.55 | 52.60 | 52.84 | 52.71 | 0.10 |
| Sb | 0.01 | 0.02 | 0.01 | 0.00 | 0.00 | 0.40 | 0.07 | 0.10 | 0.01 | 0.02 | 0.02 | 0.00 |
| Fe | 58.69 | 59.92 | 59.48 | 0.37 | 44.94 | 46.69 | 45.98 | 0.44 | 45.61 | 46.33 | 46.05 | 0.31 |
| Co | 0.03 | 0.05 | 0.05 | 0.01 | 0.01 | 0.04 | 0.02 | 0.01 | 0.02 | 0.04 | 0.03 | 0.01 |
| Ni | 0.00 | 0.05 | 0.01 | 0.02 | 0.00 | 0.02 | 0.00 | 0.01 | 0.00 | 0.00 | 0.00 | 0.00 |
| Cu | 0.00 | 0.09 | 0.03 | 0.03 | 0.00 | 0.10 | 0.01 | 0.02 | 0.01 | 0.10 | 0.05 | 0.03 |
| Zn | 0.00 | 0.02 | 0.01 | 0.01 | 0.00 | 0.18 | 0.03 | 0.03 | 0.02 | 0.04 | 0.03 | 0.01 |
| As | 0.00 | 0.03 | 0.01 | 0.01 | 0.00 | 1.15 | 0.20 | 0.27 | 0.01 | 0.03 | 0.02 | 0.01 |
| Total | 97.37 | 98.84 | 98.29 | 0.46 | 97.74 | 100.67 | 99.29 | 0.71 | 98.7 | 99.2 | 98.9 | 0.18 |
| At.% | | | | | | | | | | | | |
| Au | 0.00 | 0.01 | 0.01 | 0.00 | 0.00 | 0.01 | 0.01 | 0.00 | 0.00 | 0.01 | 0.00 | 0.00 |
| Ag | 0.00 | 0.01 | 0.01 | 0.00 | 0.00 | 0.02 | 0.01 | 0.00 | 0.00 | 0.01 | 0.00 | 0.00 |
| S | 52.35 | 54.17 | 53.02 | 0.54 | 66.16 | 66.96 | 66.57 | 0.22 | 66.39 | 66.69 | 66.50 | 0.13 |
| Sb | 0.00 | 0.01 | 0.01 | 0.00 | 0.00 | 0.13 | 0.02 | 0.03 | 0.00 | 0.01 | 0.01 | 0.00 |
| Fe | 45.72 | 47.53 | 46.86 | 0.53 | 32.94 | 33.53 | 33.21 | 0.17 | 33.06 | 33.52 | 33.36 | 0.21 |
| Co | 0.02 | 0.04 | 0.03 | 0.00 | 0.01 | 0.03 | 0.01 | 0.00 | 0.01 | 0.02 | 0.02 | 0.00 |
| Ni | 0.00 | 0.04 | 0.01 | 0.01 | 0.00 | 0.01 | 0.00 | 0.00 | 0.00 | 0.00 | 0.00 | 0.00 |
| Cu | 0.00 | 0.06 | 0.02 | 0.02 | 0.00 | 0.07 | 0.01 | 0.01 | 0.01 | 0.06 | 0.03 | 0.02 |
| Zn | 0.00 | 0.01 | 0.01 | 0.01 | 0.00 | 0.11 | 0.02 | 0.02 | 0.01 | 0.03 | 0.02 | 0.01 |
| As | 0.00 | 0.02 | 0.01 | 0.01 | 0.00 | 0.63 | 0.11 | 0.15 | 0.00 | 0.02 | 0.01 | 0.00 |

A: Pyrrhotite; B: Idiomorphic marcasite; C: Non-idiomorphic marcasite; $n$: number of analyses; Min: minimum; Max: maximum; Ave: average; s.d.: standard deviation

grain size: fine- (<20 μm) and medium- to coarse-grained (>20 μm) pyrites.

Tables 2 and 3 display the results of pyrite analyses obtained by EPMA. Among the trace elements, As has significant concentrations of up to 6.11 wt.%. Other elements have lower concentrations, rarely exceeding 1 wt.%. There are notable differences in the compositions of the textural varieties of medium–coarse and fine-grained pyrites, as noted below.

Table 4 presents the large acquisition-time analyses for Au in different types of pyrite, these always being less than the detection limit, 450 ppm, even in the As-rich pyrites.

### *Medium- to coarse-grained pyrite (>20 μm)*

Generally these pyrites are disseminated in the volcanic host rocks, in zones of massive silicification and in quartz veins. In the veins, the pyrite aggregates may display diverse textures: disseminations, stockwork-like veinlets, brecciated, crustiform and massive aggregates. There are three main morphologies of idiomorphic and subidiomorphic pyrites: cubic (with or without striations), pentagonal dodecahedral, and octahedral (Fig. 5). The pentagonal dodecahedral morphology is ubiquitous throughout the deposit; the octahedral morphology is related to near surface, native gold-bearing massively silicified zones; and the cubic morphology occurs in the veins related to deep seated, Au-Ag alloy-bearing zones.

These pyrites may be differentiated into at least four chemical types: As-bearing pyrites (type I), Co-Ni-bearing pyrites (type II), Cu-Ag bearing pyrites (type III), as well as pyrite which is lacking in trace elements (type IV).

#### *Type I: As-bearing pyrite*

This type of pyrite is found only within pentagonal dodecahedral or xenomorphic crystals, in which As is enriched in cores (up to 400 μm in diameter) as well as in polygonal to irregular bands (<20 μm in thickness).

The cores can be compact or porous (Fig. 6*a*) and occasionally show complex irregular textures

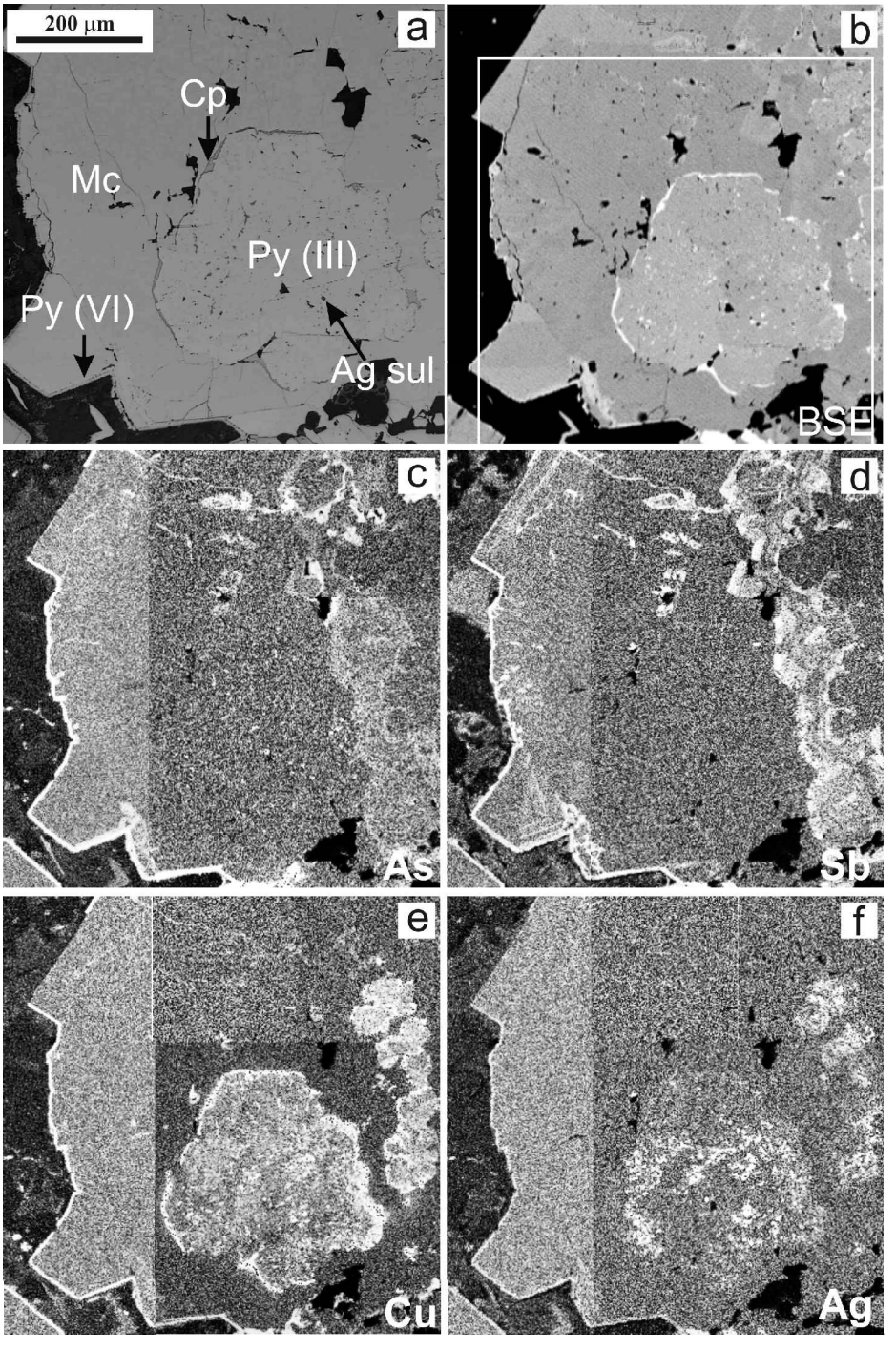


FIG. 3. Photomicrograph (*a*), backscattered electron (BSE) (*b*) and X-ray images of As (*c*), Sb (*d*), Cu (*e*) and Ag (*f*) of the association type III pyrite (Py III) with Ag sulphide inclusions (Ag sul), chalcopyrite (Cp), idiomorphic marcasite (Mc) and collomorphic pyrite (Py VI).

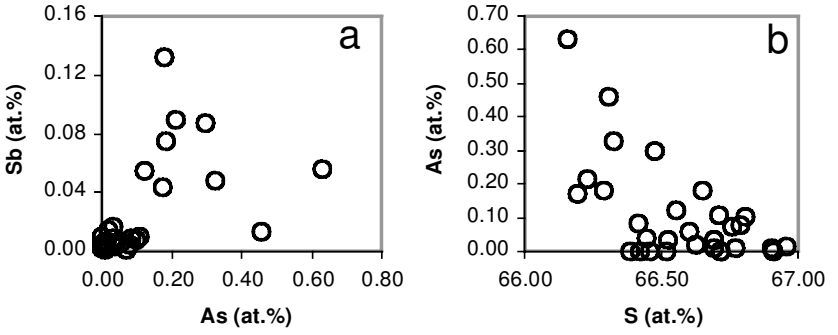


FIG. 4. (*a*) As *vs*. Sb diagram showing the relationship between both elements in idiomorphic marcasite. (*b*) S *vs*. As diagram showing the inverse correlation between As and S in idiomorphic marcasite.

(Fig. 6*b*) in which tiny crystals of arsenopyrite can sometimes be found.

Polygonal bands are scarce and occur as pentagonal dodecahedrons or cubes (Figs 6*a* and 7*a*). These bands, which occasionally contain tennantite crystals (Fig. 6*a*), are thin (1–2 μm), with clear boundaries, although they occasionally group together, thus appearing to be thicker.

Irregular bands (Fig. 7*b*) are more common than the polygonal bands and are more diffuse. They show continuous variations in thickness, frequent truncations and features typical of dissolution or uneven growth. They are normally found in the internal parts of the crystals, rarely in the rims.

In contrast with other deposits (e.g. Fleet *et al*., 1989), where oscillatory As zoning affects the entire pyrite crystal, the As enrichment (type I pyrite), is restricted mainly to the most internal parts of the pyrite grains. This type of pyrite can be dissolved and overgrown by coarse pyrite lacking trace elements (Fig. 7*b*).

The chemistry of type I pyrite (Table 2) is characterized by a clear enrichment in As (up to 3.38 wt.%), negatively correlated with S (Fig. 8a) whereas no correlation exists between As and Fe (Fig. 8*b*). In some cases there is a sporadic increase in Cu (up to 0.19%), particularly in the cores (Fig. 6*a,b*). Figure 8*c* shows that (1) the As values in the cores are lower than in the bands and (2) the irregular bands are poorer in As than the polygonal bands.

### *Type II: Co-Ni-bearing pyrite*

This type of pyrite, detectable only by X-ray maps, is prior to or occasionally coeval with As-bearing, type I pyrite. The type II pyrite (Table 2) is found in the internal parts of the pyrite crystals lacking trace elements, as Co- or Ni-cores or bands (Fig. 7*a,b*). This type shows the highest Co (0.01–0.69 wt.%) and Ni (0.00–1.01 wt.%) values and an increase in these elements involves a slight decrease in the Fe content of pyrite.

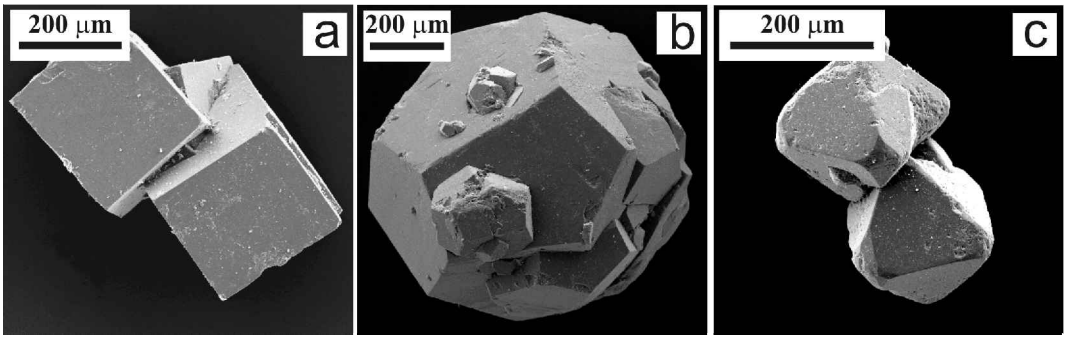


FIG. 5. SEM secondary electron images showing pyrite morphology: (*a*) cubic habit, (*b*) pentagonal dodecahedral habit and (*c*) octahedral habit.

TABLE 2. Chemistry of medium- to coarse-grained pyrite (>20 μm).

| | A ($n$ = 19) | | | | B ($n$ = 21) | | | | C ($n$ = 39) | | | | D ($n$ = 37) | | | | E ($n$ = 18) | | | | F ($n$ = 107) | | | |
|---|---|---|---|---|---|---|---|---|---|---|---|---|---|---|---|---|---|---|---|---|---|---|---|---|
| Wt.% | Min. | Max. | Ave. | s.d. (1σ) | Min. | Max. | Ave. | s.d. (1σ) | Min. | Max. | Ave. | s.d. (1σ) | Min. | Max. | Ave. | s.d. (1σ) | Min. | Max. | Ave. | s.d. (1σ) | Min. | Max. | Ave. | s.d. (1σ) |
| Au | 0.00 | 0.16 | 0.03 | 0.04 | 0.00 | 0.06 | 0.03 | 0.02 | 0.00 | 0.16 | 0.03 | 0.03 | 0.00 | 0.05 | 0.02 | 0.01 | 0.00 | 0.05 | 0.02 | 0.01 | 0.00 | 0.10 | 0.02 | 0.02 |
| Ag | 0.00 | 0.06 | 0.01 | 0.01 | 0.00 | 0.03 | 0.01 | 0.01 | 0.00 | 0.09 | 0.02 | 0.02 | 0.00 | 0.05 | 0.01 | 0.01 | 0.00 | 1.47 | 0.18 | 0.35 | 0.00 | 0.17 | 0.02 | 0.02 |
| S | 51.31 | 53.03 | 52.16 | 0.43 | 50.50 | 52.62 | 51.59 | 0.64 | 49.39 | 53.61 | 52.10 | 0.78 | 50.87 | 53.83 | 52.72 | 0.79 | 52.07 | 53.53 | 52.79 | 0.44 | 51.55 | 54.85 | 53.30 | 0.54 |
| Sb | 0.00 | 0.03 | 0.01 | 0.01 | 0.00 | 0.11 | 0.02 | 0.02 | 0.00 | 0.19 | 0.03 | 0.04 | 0.00 | 0.04 | 0.01 | 0.01 | 0.00 | 0.04 | 0.01 | 0.01 | 0.00 | 0.06 | 0.01 | 0.01 |
| Fe | 45.38 | 46.56 | 46.10 | 0.32 | 44.39 | 46.06 | 45.33 | 0.53 | 44.51 | 46.75 | 46.05 | 0.49 | 44.39 | 46.41 | 45.66 | 0.60 | 44.42 | 46.52 | 45.78 | 0.52 | 44.68 | 46.98 | 46.19 | 0.43 |
| Co | 0.00 | 0.09 | 0.03 | 0.02 | 0.02 | 0.51 | 0.17 | 0.16 | 0.00 | 0.07 | 0.02 | 0.01 | 0.01 | 0.69 | 0.25 | 0.19 | 0.01 | 0.03 | 0.02 | 0.01 | 0.00 | 0.12 | 0.03 | 0.02 |
| Ni | 0.00 | 0.03 | 0.00 | 0.01 | 0.00 | 0.90 | 0.17 | 0.27 | 0.00 | 0.05 | 0.01 | 0.01 | 0.00 | 1.01 | 0.21 | 0.26 | 0.00 | 0.01 | 0.00 | 0.00 | 0.00 | 0.08 | 0.01 | 0.01 |
| Cu | 0.00 | 0.19 | 0.02 | 0.04 | 0.00 | 0.16 | 0.02 | 0.03 | 0.00 | 0.14 | 0.02 | 0.03 | 0.00 | 0.08 | 0.01 | 0.02 | 0.01 | 0.62 | 0.20 | 0.16 | 0.00 | 0.70 | 0.04 | 0.11 |
| Zn | 0.00 | 0.30 | 0.03 | 0.07 | 0.00 | 0.02 | 0.01 | 0.01 | 0.00 | 0.04 | 0.01 | 0.01 | 0.00 | 0.04 | 0.01 | 0.01 | 0.00 | 0.04 | 0.01 | 0.01 | 0.00 | 0.39 | 0.02 | 0.04 |
| As | 0.24 | 2.27 | 0.99 | 0.66 | 1.03 | 3.38 | 2.27 | 0.60 | 0.28 | 2.76 | 1.28 | 0.80 | 0.00 | 3.38 | 0.83 | 1.18 | 0.00 | 0.10 | 0.02 | 0.02 | 0.00 | 0.23 | 0.04 | 0.05 |
| Total | 97.78 | 100.09 | 99.32 | 0.63 | 98.51 | 100.67 | 99.62 | 0.56 | 93.94 | 100.52 | 99.33 | 1.10 | 98.96 | 100.63 | 99.73 | 0.37 | 96.52 | 102.40 | 99.03 | 1.53 | 98.20 | 102.48 | 99.97 | 0.80 |
| At.% | | | | | | | | | | | | | | | | | | | | | | | | |
| Au | 0.00 | 0.03 | 0.01 | 0.01 | 0.00 | 0.01 | 0.01 | 0.00 | 0.00 | 0.03 | 0.00 | 0.0 | 0.00 | 0.01 | 0.00 | 0.00 | 0.00 | 0.01 | 0.00 | 0.00 | 0.00 | 0.02 | 0.00 | 0.00 |
| Ag | 0.00 | 0.02 | 0.01 | 0.01 | 0.00 | 0.01 | 0.01 | 0.00 | 0.00 | 0.04 | 0.01 | 0.0 | 0.00 | 0.02 | 0.01 | 0.00 | 0.00 | 0.56 | 0.07 | 0.13 | 0.00 | 0.06 | 0.01 | 0.01 |
| S | 65.44 | 66.50 | 65.93 | 0.29 | 64.69 | 66.26 | 65.45 | 0.41 | 64.91 | 66.77 | 65.87 | 0.4 | 64.92 | 66.88 | 66.24 | 0.58 | 66.32 | 66.83 | 66.58 | 0.16 | 65.83 | 67.36 | 66.70 | 0.32 |
| Sb | 0.00 | 0.01 | 0.00 | 0.00 | 0.00 | 0.04 | 0.01 | 0.01 | 0.00 | 0.06 | 0.01 | 0.0 | 0.00 | 0.01 | 0.00 | 0.00 | 0.00 | 0.01 | 0.00 | 0.00 | 0.00 | 0.02 | 0.00 | 0.00 |
| Fe | 33.07 | 33.85 | 33.45 | 0.20 | 32.21 | 33.94 | 33.02 | 0.43 | 32.92 | 34.27 | 33.43 | 0.3 | 32.14 | 33.48 | 32.94 | 0.31 | 32.54 | 33.51 | 33.15 | 0.21 | 32.38 | 34.08 | 33.19 | 0.32 |
| Co | 0.00 | 0.06 | 0.02 | 0.01 | 0.01 | 0.35 | 0.11 | 0.11 | 0.00 | 0.04 | 0.01 | 0.0 | 0.00 | 0.46 | 0.17 | 0.13 | 0.01 | 0.02 | 0.01 | 0.00 | 0.00 | 0.08 | 0.01 | 0.01 |
| Ni | 0.00 | 0.02 | 0.00 | 0.01 | 0.00 | 0.62 | 0.12 | 0.18 | 0.00 | 0.04 | 0.00 | 0.0 | 0.00 | 0.70 | 0.15 | 0.18 | 0.00 | 0.01 | 0.00 | 0.00 | 0.00 | 0.05 | 0.01 | 0.01 |
| Cu | 0.00 | 0.13 | 0.01 | 0.03 | 0.00 | 0.11 | 0.01 | 0.02 | 0.00 | 0.09 | 0.01 | 0.0 | 0.00 | 0.05 | 0.01 | 0.01 | 0.01 | 0.40 | 0.13 | 0.10 | 0.00 | 0.44 | 0.02 | 0.07 |
| Zn | 0.00 | 0.18 | 0.02 | 0.04 | 0.00 | 0.01 | 0.01 | 0.01 | 0.00 | 0.02 | 0.01 | 0.0 | 0.00 | 0.02 | 0.01 | 0.01 | 0.00 | 0.02 | 0.01 | 0.01 | 0.00 | 0.24 | 0.01 | 0.03 |
| As | 0.13 | 1.23 | 0.53 | 0.35 | 0.56 | 1.84 | 1.23 | 0.33 | 0.15 | 1.51 | 0.63 | 0.43 | 0.00 | 1.84 | 0.45 | 0.64 | 0.00 | 0.05 | 0.01 | 0.01 | 0.00 | 0.12 | 0.02 | 0.03 |

A: type I (cores); B: type I (polygonal bands); C: type I (irregular bands); D: type II; E: type III; F: type IV; $n$: number of analyses; Min: minimum; Max: maximum; Ave: average; s.d.: standard deviation

TABLE 3. Chemistry of fine-grained pyrite (<20 μm).

| | A ($n$ = 17) | | | | B ($n$ = 9) | | | | C ($n$ = 18) | | | | D ($n$ = 33) | | | | E ($n$ = 11) | | | | F ($n$ = 13) | | | |
|---|---|---|---|---|---|---|---|---|---|---|---|---|---|---|---|---|---|---|---|---|---|---|---|---|
| Wt.% | Min. | Max. | Ave. | s.d. (1σ) | Min. | Max. | Ave. | s.d. (1σ) | Min. | Max. | Ave. | s.d. (1σ) | Min. | Max. | Ave. | s.d. (1σ) | Min. | Max. | Ave. | s.d. (1σ) | Min. | Max. | Ave. | s.d. (1σ) |
| Au | 0.00 | 0.06 | 0.03 | 0.01 | 0.00 | 0.05 | 0.02 | 0.02 | 0.00 | 0.04 | 0.02 | 0.01 | 0.00 | 0.05 | 0.02 | 0.01 | 0.00 | 0.04 | 0.02 | 0.01 | 0.00 | 0.05 | 0.02 | 0.01 |
| Ag | 0.00 | 0.06 | 0.03 | 0.02 | 0.00 | 0.06 | 0.02 | 0.02 | 0.00 | 0.16 | 0.07 | 0.05 | 0.00 | 0.20 | 0.04 | 0.04 | 0.00 | 0.05 | 0.02 | 0.01 | 0.00 | 0.08 | 0.03 | 0.03 |
| S | 52.46 | 53.79 | 53.23 | 0.36 | 48.60 | 53.09 | 51.86 | 1.45 | 50.25 | 53.08 | 51.85 | 0.68 | 49.62 | 53.79 | 51.45 | 1.21 | 51.75 | 53.46 | 52.68 | 0.57 | 51.75 | 53.66 | 53.06 | 0.53 |
| Sb | 0.01 | 0.03 | 0.02 | 0.01 | 0.00 | 0.02 | 0.01 | 0.01 | 0.07 | 0.46 | 0.18 | 0.08 | 0.00 | 1.41 | 0.30 | 0.42 | 0.00 | 0.03 | 0.01 | 0.01 | 0.00 | 0.08 | 0.02 | 0.02 |
| Fe | 44.53 | 46.52 | 45.91 | 0.43 | 41.11 | 45.43 | 44.19 | 1.44 | 41.93 | 46.16 | 44.50 | 1.19 | 41.61 | 46.29 | 43.73 | 1.42 | 45.68 | 46.62 | 46.27 | 0.24 | 45.27 | 46.33 | 45.73 | 0.37 |
| Co | 0.01 | 0.05 | 0.02 | 0.01 | 0.04 | 0.10 | 0.07 | 0.02 | 0.01 | 0.04 | 0.02 | 0.01 | 0.00 | 0.04 | 0.02 | 0.01 | 0.01 | 0.05 | 0.03 | 0.01 | 0.01 | 0.03 | 0.02 | 0.01 |
| Ni | 0.00 | 0.02 | 0.00 | 0.01 | 0.01 | 0.11 | 0.04 | 0.03 | 0.00 | 0.14 | 0.05 | 0.05 | 0.00 | 0.01 | 0.00 | 0.00 | 0.00 | 0.04 | 0.01 | 0.01 | 0.00 | 0.08 | 0.02 | 0.03 |
| Cu | 0.00 | 0.05 | 0.02 | 0.01 | 0.00 | 0.02 | 0.00 | 0.01 | 0.00 | 0.94 | 0.25 | 0.27 | 0.00 | 1.26 | 0.19 | 0.27 | 0.01 | 0.39 | 0.13 | 0.11 | 0.00 | 1.32 | 0.57 | 0.39 |
| Zn | 0.00 | 0.03 | 0.01 | 0.01 | 0.00 | 0.02 | 0.01 | 0.01 | 0.00 | 0.18 | 0.06 | 0.06 | 0.00 | 0.10 | 0.01 | 0.02 | 0.00 | 0.07 | 0.02 | 0.02 | 0.00 | 0.19 | 0.04 | 0.05 |
| As | 0.11 | 0.66 | 0.21 | 0.13 | 0.00 | 0.29 | 0.11 | 0.08 | 0.53 | 4.49 | 2.36 | 1.10 | 0.08 | 6.11 | 3.76 | 1.84 | 0.00 | 0.08 | 0.02 | 0.03 | 0.00 | 0.12 | 0.02 | 0.03 |
| Total | 97.44 | 100.64 | 99.50 | 0.73 | 89.96 | 98.76 | 96.33 | 2.91 | 98.20 | 100.44 | 99.37 | 0.58 | 98.06 | 100.56 | 99.53 | 0.71 | 97.95 | 99.92 | 99.22 | 0.58 | 98.06 | 100.92 | 99.53 | 0.93 |
| At.% | | | | | | | | | | | | | | | | | | | | | | | | |
| Au | 0.00 | 0.01 | 0.01 | 0.00 | 0.00 | 0.01 | 0.00 | 0.00 | 0.00 | 0.01 | 0.00 | 0.00 | 0.00 | 0.01 | 0.00 | 0.00 | 0.00 | 0.01 | 0.00 | 0.00 | 0.00 | 0.01 | 0.00 | 0.00 |
| Ag | 0.00 | 0.02 | 0.01 | 0.01 | 0.00 | 0.02 | 0.01 | 0.01 | 0.00 | 0.06 | 0.03 | 0.02 | 0.00 | 0.08 | 0.02 | 0.02 | 0.00 | 0.02 | 0.01 | 0.00 | 0.00 | 0.03 | 0.01 | 0.01 |
| S | 66.45 | 67.20 | 66.75 | 0.19 | 66.73 | 67.28 | 67.02 | 0.18 | 65.27 | 66.65 | 65.88 | 0.30 | 64.75 | 66.93 | 65.62 | 0.64 | 66.03 | 66.77 | 66.35 | 0.26 | 66.05 | 66.97 | 66.58 | 0.29 |
| Sb | 0.00 | 0.01 | 0.01 | 0.00 | 0.00 | 0.01 | 0.00 | 0.00 | 0.03 | 0.15 | 0.06 | 0.03 | 0.00 | 0.49 | 0.10 | 0.14 | 0.00 | 0.01 | 0.00 | 0.00 | 0.00 | 0.03 | 0.01 | 0.01 |
| Fe | 32.64 | 33.28 | 33.05 | 0.17 | 32.52 | 33.03 | 32.79 | 0.18 | 31.27 | 33.20 | 32.46 | 0.60 | 31.18 | 33.08 | 32.01 | 0.61 | 33.09 | 33.79 | 33.47 | 0.25 | 32.61 | 33.89 | 32.95 | 0.35 |
| Co | 0.00 | 0.03 | 0.01 | 0.01 | 0.02 | 0.07 | 0.05 | 0.02 | 0.01 | 0.03 | 0.01 | 0.01 | 0.00 | 0.02 | 0.01 | 0.01 | 0.00 | 0.03 | 0.02 | 0.01 | 0.00 | 0.02 | 0.01 | 0.01 |
| Ni | 0.00 | 0.01 | 0.00 | 0.00 | 0.01 | 0.08 | 0.03 | 0.02 | 0.00 | 0.10 | 0.03 | 0.04 | 0.00 | 0.01 | 0.00 | 0.00 | 0.00 | 0.03 | 0.01 | 0.01 | 0.00 | 0.05 | 0.01 | 0.02 |
| Cu | 0.00 | 0.03 | 0.01 | 0.01 | 0.00 | 0.01 | 0.00 | 0.00 | 0.00 | 0.61 | 0.16 | 0.17 | 0.00 | 0.83 | 0.13 | 0.18 | 0.01 | 0.25 | 0.08 | 0.07 | 0.00 | 0.83 | 0.36 | 0.25 |
| Zn | 0.00 | 0.02 | 0.01 | 0.01 | 0.00 | 0.02 | 0.01 | 0.01 | 0.00 | 0.11 | 0.04 | 0.03 | 0.00 | 0.06 | 0.01 | 0.01 | 0.00 | 0.04 | 0.01 | 0.01 | 0.00 | 0.12 | 0.02 | 0.03 |
| As | 0.06 | 0.35 | 0.12 | 0.07 | 0.00 | 0.16 | 0.06 | 0.05 | 0.29 | 2.50 | 1.29 | 0.61 | 0.04 | 3.36 | 2.06 | 1.02 | 0.00 | 0.05 | 0.01 | 0.01 | 0.00 | 0.07 | 0.01 | 0.02 |

A: type V (framboids *sensu stricto*); B: type V (pseudoframboids); C: type VI (collomorphic porous pyrite); D: type VI (brown collomorphic pyrite); E: type VII (micro-geodes); F: type VII (pyrite intergrowths in chalcopyrite); $n$: number of analyses; Min: minimum; Max: maximum; Ave: average; s.d.: standard deviation

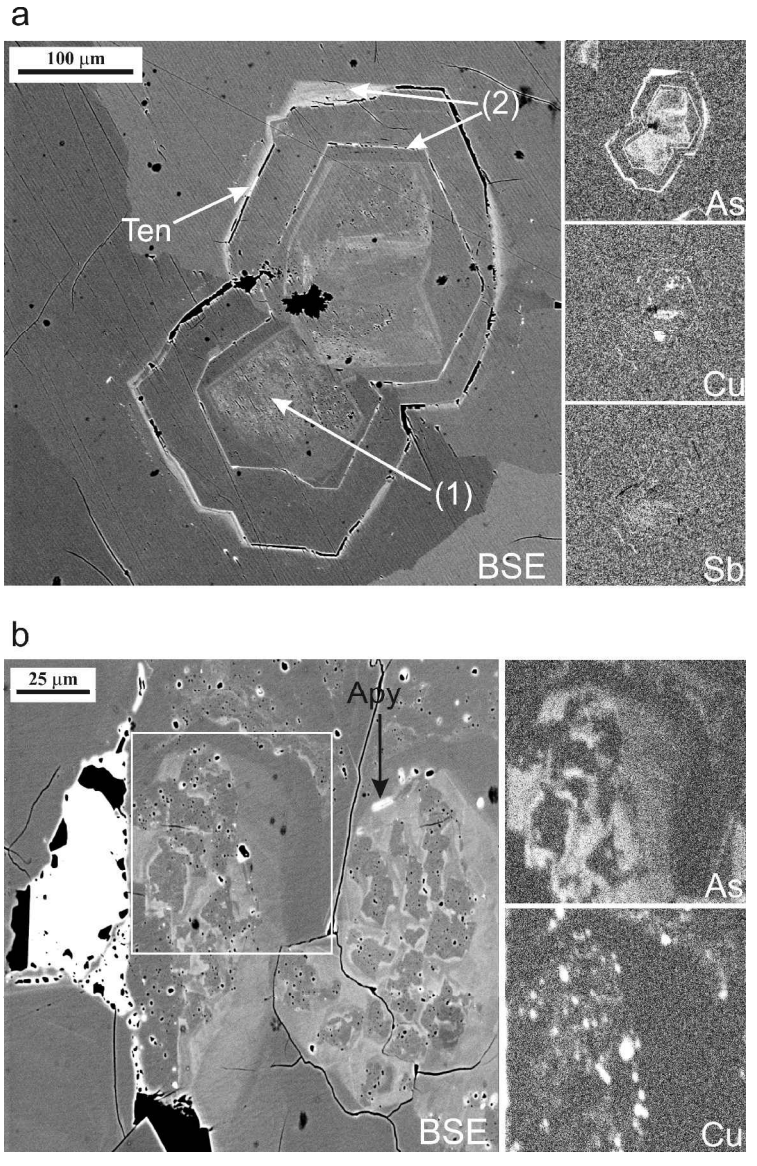


FIG. 6. (*a*) BSE and X-ray images of As-rich type I pyrite overgrown by nearly stoichiometric pyrite type IV: (1) core of type I pyrite with porous character (dark areas); (2) thin polygonal bands of type I pyrite with a tennantite (Ten) inclusion. On the right hand side of the figure note the As, Cu and Sb X-ray images, where Cu and Sb are slightly enriched in the type I pyrite core. (*b*) BSE and X-ray images of As-rich, type I pyrite core with a complex texture and a tiny arsenopyrite inclusion (Apy). On the right hand side of the figure note the As and Cu X-ray images from the marked area.

### *Type III: pyrite with Cu and Ag*

Associated with idiomorphic marcasite in the above-described marcasite, there are pyrites (Table 2) which have significant amounts of Cu (up to 0.62 wt.%) and Ag (up to 1.47 wt.%). Figure 3*e* and *f* shows extended enrichments of Cu and minor in Ag throughout all pyrite grains whereas in Fig. 9 we observed that the Cu and Ag levels are approximately equal with a 'background' of Cu of 0.10 at.%.

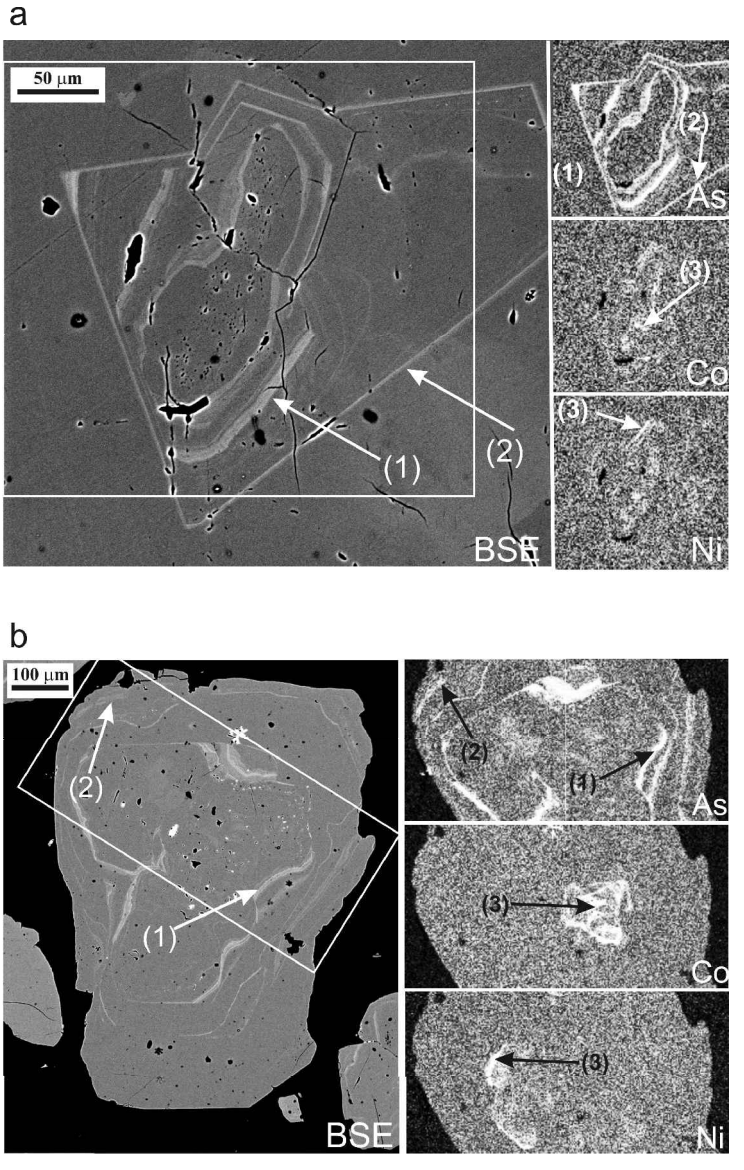


FIG. 7. (*a*) BSE and X-ray images of type I (As-bearing) and type II (Co-Ni-bearing) pyrite hosted by type IV pyrite: (1) polygonal bands of type I pyrite with a pentagonal dodecahedral morphology overgrown by (2) a polygonal band with cubic morphology. As, Co and Ni X-ray images, on the right hand side of the figure, reveal Co-Ni bearing, type II pyrite in core and bands (3). (*b*) BSE and X-ray images of type I (As-bearing) and type II (Co-Ni-bearing) pyrite hosted by type IV pyrite: (1) irregular bands of type I with abundant truncations in the inner part of the crystal; (2) irregular bands of type I in the rim of the crystal. On the right hand side of the figure note the As, Co and Ni X-ray images, with the non-coincident Co-rich and Ni-rich pyrite (3).

*Type IV: pyrite 'lacking' trace elements*

This type of pyrite, volumetrically the most abundant, is characterized by neglible concentrations of trace elements (Table 2). Type IV pyrite is found as disseminations throughout the volcanic host rock or in quartz veins and silicified zones where it can contain types I and II pyrites or else appear as homogeneous crystals. Type IV pyrite

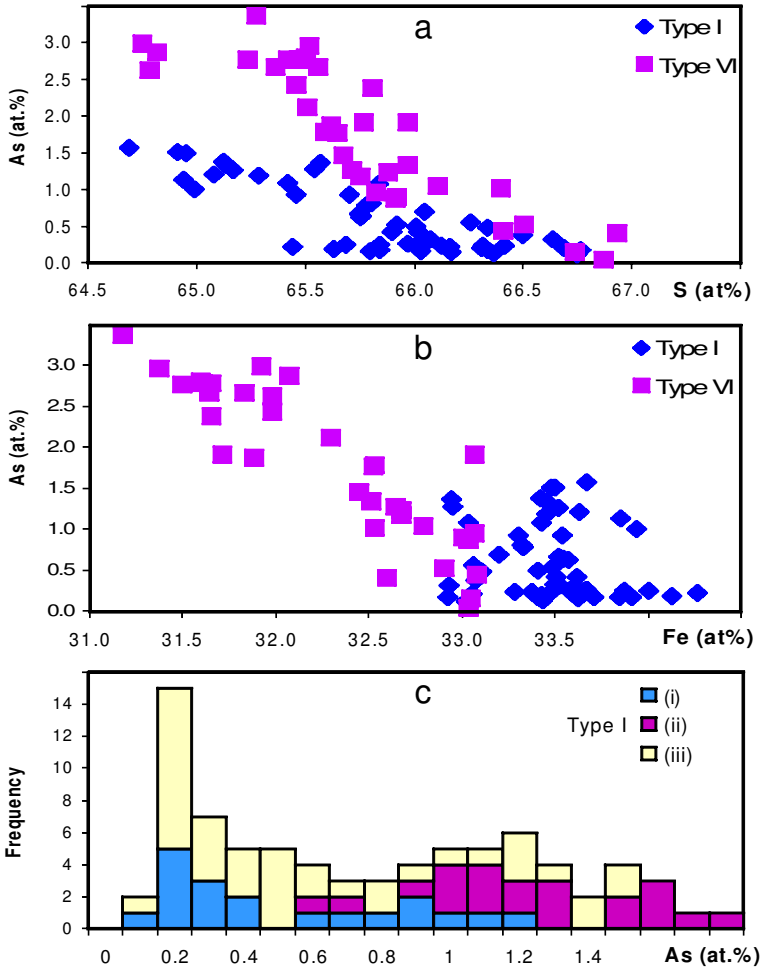


FIG. 8. (*a*) S *vs*. As diagram showing inverse correlation, with different slopes for type I and type VI pyrite. (*b*) Fe *vs*. As diagram showing no correlation in type I pyrite, but good inverse correlation in type VI pyrite. (*c*) Arsenic content frequency histogram in type I pyrite: (i) cores; (ii) polygonal bands; (iii) irregular bands. Observe that the cores have the lowest As content while the highest As values are in the polygonal bands.

frequently has pore-rich zones that generally coincide with the central parts of the crystals, which also have high concentrations of mineral microinclusions, especially pyrrhotite, chalcopyrite, rutile and magnetite.

It should be noted that Au-Ag alloys are hosted by the type IV pyrite, preferentially included in the pore-free zones (Fig. 2*a*).

### *Fine-grained pyrites (<20 μm)*

This group comprises framboidal (type V) and collomorphic (type VI) pyrites, as well as microgeodes and intergrowths of pyrite in chalcopyrite (type VII).

#### *Type V: framboidal pyrite*

This type is relatively rare and occurs in two varieties: (1) As framboids *sensu stricto* (Fig. 10*a*), generally spherical and <50 μm in size. The pyrite microcrystals, very closely packed, are subidiomorphic and equigranular (±2 μm). In some cases, the framboidal pyrite is overgrown by coarse-grained type IV pyrite. (2) As 'pseudoframboids' (Fig. 10*b*) that are loosely packed or even disaggregated, with sizes

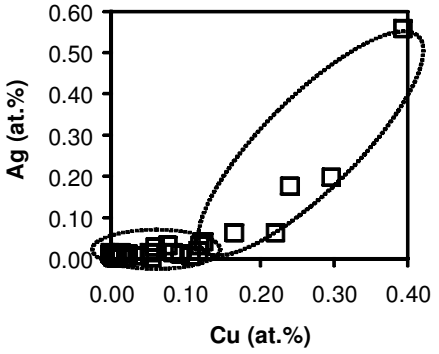


FIG. 9. (*a*) Cu *vs*. Ag diagram showing two types of behaviour (represented by ellipses) of the relation between both elements in type III pyrite.

of up to 50 μm. In contrast to the framboids *sensu stricto*, the pyrite microcrystals here are rounded or oval-shaped and vary in size from <1 to 5 μm. The outermost crystals are the largest.

Both types of framboidal pyrites show small amounts of trace elements, As being the most abundant (average of 0.18 wt.%, Table 3).

*Type VI: collomorphic pyrite*

These pyrites occur principally in two generations of overgrowth on previous pyrite crystals, although they can also overgrow idiomorphic marcasite and, exceptionally, chalcopyrite. Type VI occurs as either porous collomorphic pyrite (Fig. 10*c*), or as brown collomorphic pyrite under reflected light microscope (Fig. 10*d*).

These pyrites have the largest amounts of As (0.08–6.11 wt.%), Cu (0.00–1.26 wt.%), Sb (0.00–1.41 wt.%) and Ag (0.00–0.20 wt.%), but the smallest Fe contents (41.9–46.2 wt.%) of all the pyrites analysed in the deposit. Nickel and Zn have also been detected (Table 3). Arsenic is negatively correlated with S, with a slope (–1.58) more pronounced than for the type I pyrite (Fig. 8a). The As is also negatively correlated with Fe (Fig. 8*b*).

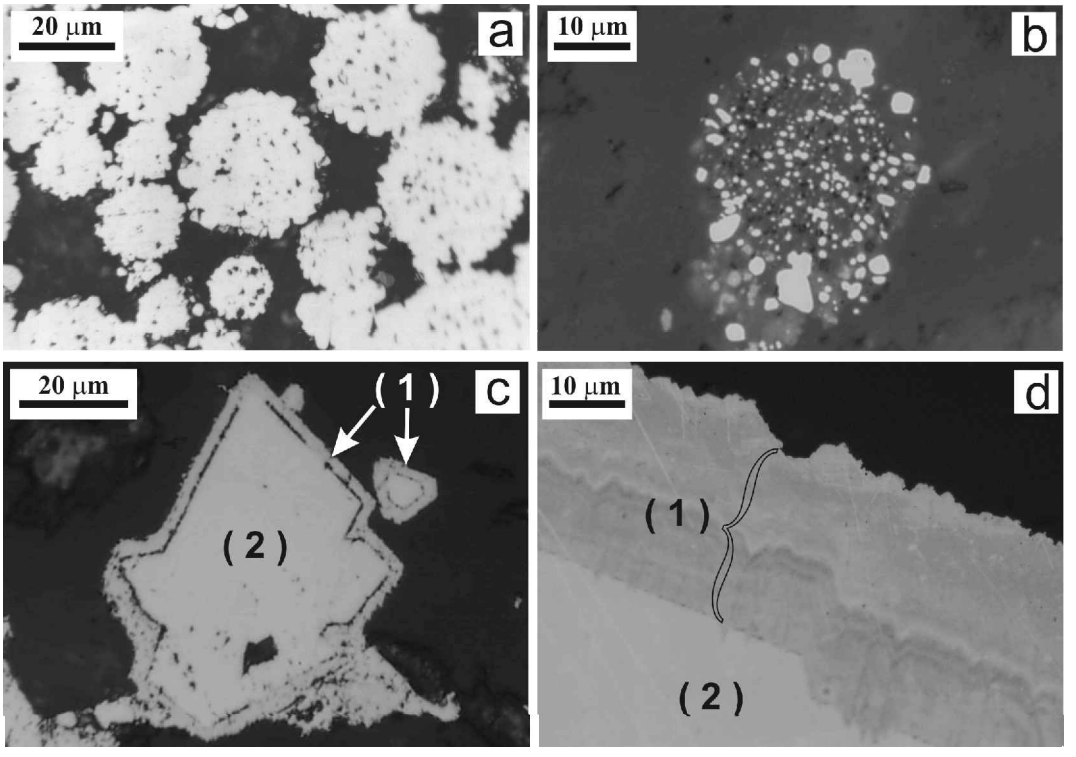


FIG. 10. Photomicrographs of type V and type VI pyrite. (*a*) Framboids *sensu stricto* closely packed with subidiomorphic, coalescing microcrystals. (*b*) 'Pseudoframboid' of loosely packed pyrite of rounded or oval shapes. (*c*) Porous collomorphic pyrite (1) overgrowing marcasite and coarse pyrite (2). (*d*) Bands of brown collomorphic pyrite showing graded shading (1) overgrowing coarse pyrite (2).

Within the overgrowths of collomorphic pyrite, the first generation is usually richer in As than the second one (Fig. 11*a*,*b*), with some chemical differences between the two textural varieties.

The porous collomorphic pyrite contains less As (0.53–4.49 wt.%) than the brown collomorphic pyrite. It also has relatively large amounts of Ag, Cu, Ni and Zn, and these are directly correlated with As concentration (Fig. 12), a feature that is evident from the X-ray maps in Fig. 10*a* for Cu, Ag and Ni.

The brown collomorphic pyrite has the highest As content (0.08–6.11 wt.%). It is is also enriched in Ag, Cu and Sb, but not in Zn or Ni. In contrast with the porous variety, there is no direct correlation between these elements and As (Fig. 12). However, at high As concentrations, there is an enrichment in Ag, Cu and Sb and the

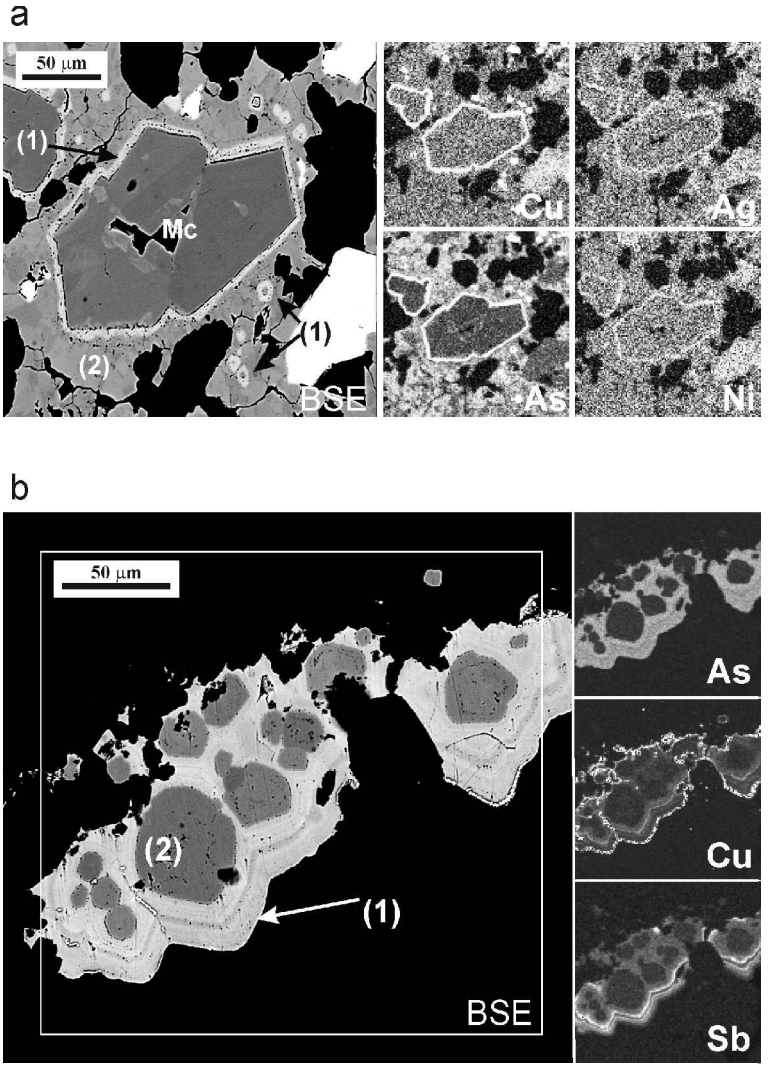


FIG. 11. (*a*) BSE and X-ray images of type VI pyrite. There are two bands, (1) and (2), of collomorphic pyrite overgrowing marcasite (Mc), with the former being richer in Cu, Ag, As and Ni than the latter. (*b*) BSE and X-ray images of type VI pyrite. Collomorphic pyrite (1) overgrowing coarse type IV pyrite (2). The As concentration is relatively homogeneous in this collomorphic pyrite, just the opposite of the Cu and Sb concentrations, which are enriched in the finer bands.

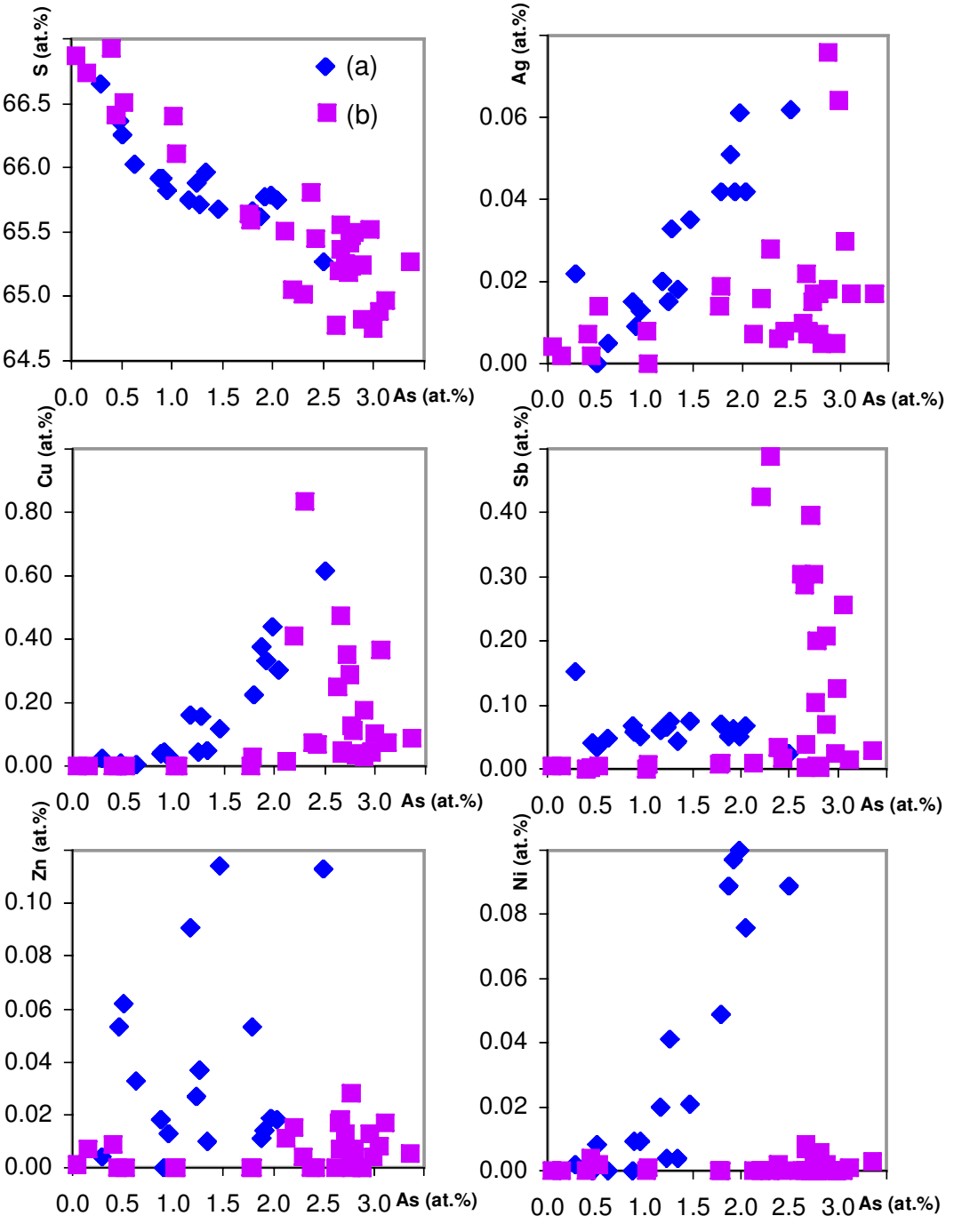


FIG. 12. Binary diagrams showing variations between different elements in type VI pyrite: (*a*) porous collomorphic pyrite and (*b*) brown collomorphic pyrite.

nature of Cu and Sb distributed in As-rich bands is shown in the X-ray maps in Fig. 11*b*.

*Type VII: pyrite micro-geodes and intergrowths in chalcopyrite*

In both cases (Fig. 13), pyrite occurs as chemically homogeneous xenomorphic fine-grained (<15 μm) aggregates located in chalcopyrite crystals. The micro-geodes tend to be up to 400 μm in diameter and sometimes host marcasite crystals. The pyrite intergrowths are distributed along elongated zones within the chalcopyrite.

The trace-element concentration is quite low in both cases, similar to that of the coarse-grained pyrite of type IV.

Based on the textural evidence summarized above, we propose a paragenetic sequence for the distinct types of Fe-sulphides at veins, presented in Fig. 14.

## Genetic considerations

*Origin of pyrite*

The pyrite of the Palai-Islica deposit originated from hydrothermal fluids. However, the formation pathways of pyrite from hydrothermal fluids are controversial, and an intermediate precursor is thought to be necessary (e.g. Benning *et al.*, 2000). Moreover, certain textural characteristics observed in the pyrite of this deposit (e.g. relics of pyrrhotite, presence of framboids), should be considered in evaluating possible processes of pyrite formation, such as (1) the transformation of pyrrhotite and marcasite and (2) the formation of pyrite framboids.

*The transformation of pyrrhotite and marcasite*

Some of the pyrite in this deposit may initially have crystallized as pyrrhotite proper and subsequently been transformed into pyrite by one of the mechanisms proposed by Fleet (1978) and by Murowchick and Barnes (1986). Due to the smaller molar volume of pyrite, this transformation could account for the existence of the high-porosity zones, particularly in the pyrite 'lacking' trace elements. Marcasite had also been a precursor of type VII pyrite as shown by the textural evidence.

*The formation of framboids*

Occasionally, the precursor of the medium- to coarse-grained pyrite may have been framboidal pyrite, which, in turn, may have had greigite as a precursor (Wilkin and Barnes, 1997). The presence of zones in the porous type IV pyrite would correspond to zones where the recrystallization was incomplete, whereas the abundant micro-inclusions in the porous pyrite could be interpreted as crystals that were trapped in the framboidal spaces. According to Wilkin and Barnes (1997), the maximum temperature at which framboidal pyrite may nucleate is 225ºC. This temperature is consistent with the lower range of temperatures determined by microthermometry of fluid inclusions (between 120 and 465ºC) in quartz associated with pyrite (Morales Ruano *et al.*, 2000).

*Evolution of As contents in the pyrite*

Pyrites in other hydrothermal deposits have characteristic oscillatory banding due to variations in a relatively continuous supply of As during precipitation (e.g. Fleet *et al.*, 1989). However, the As supply to the Palai-Islica pyrites seems to have been more episodic, concentrated in the mineralization areas, especially in relation to gold-bearing levels, but not in the hydrothermal alteration. Based on textural and mineral chemistry data, there have been two main episodes of well-defined As enrichment.

The first As-rich episode, associated with the initial stages of formation of the deposit, produced the As-rich cores and bands of type I pyrite with some related tiny crystals of arsenopyrite (main stage of pyrite precipitation). It was occasionally accompanied by the incorporation of Cu, which is sometimes linked to the formation of the tennantite inclusions. The As-rich cores and bands are the product of continuous pyrite growth, as indicated by the concentric nature of the banding, the coherence between the morphology of the banding and the crystal habits.

Following this first As-rich episode, there was a stage of As-free pyrite crystallization (type IV). The type IV pyrite is not only volumetrically significant, in places forming massive aggregates, but it also hosts gold alloys.

The second As-rich episode, associated with the final stages of the Fe sulphide deposition, is characterized by the presence of idiomorphic marcasite and two varieties of collomorphic pyrite (type VI), the most As-rich pyrites of Palai-Islica. Two consecutive bands can be distinguished, with the first one mainly richer in As.

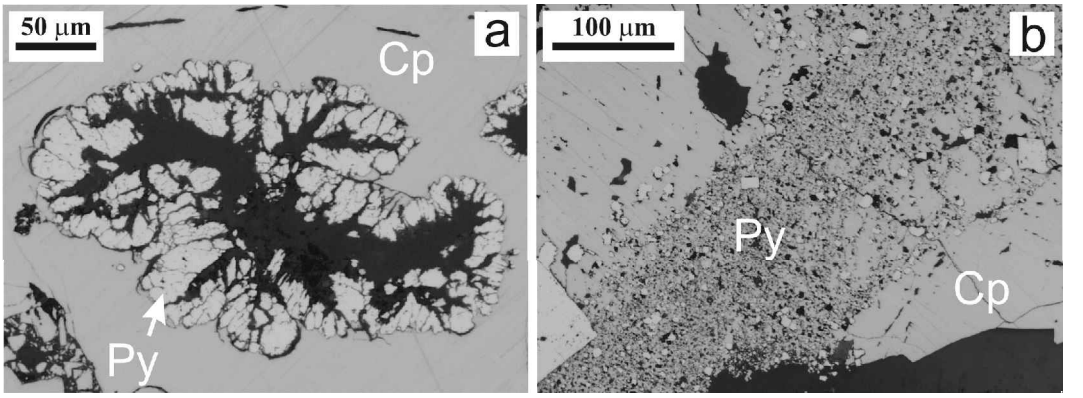


FIG. 13. Photomicrographs of type VII pyrite. (*a*) Micro-geodes of pyrite (py) in chalcopyrite (cp). (*b*) Bands of microcrystals of pyrite (py) in coarse-grained chalcopyrite (cp).

Accordingly, the As entered into the pyrite structure in two stages, and appears to be incorporated by two different mechanisms as suggested by the relationship between As, S and Fe: (1) in pyrites from the first episode, the As content of the pyrite is negatively correlated with S, while the Fe content is constant (Fig. 7*a,b*). The As was incorporated in a metastable solid solution in the S positions. It could be related to layers of 'marcasite-like' structure, with high As content (Fleet *et al.*, 1989; Simon *et al.*, 1999), or else as clusters with a lower As content in the pyrite structure (Savage *et al.*, 2000). (2) In contrast, in pyrites produced during the second episode, the As is negatively correlated with both the S and the Fe (Fig. 7*a,b*), and the increase in the As concentration is accompanied by increasing contents of Cu, Ag, Sb, Zn and Ni. In this case, there are no crystallochemical studies on the entrance of As into pyrite associated with decreasing S and Fe

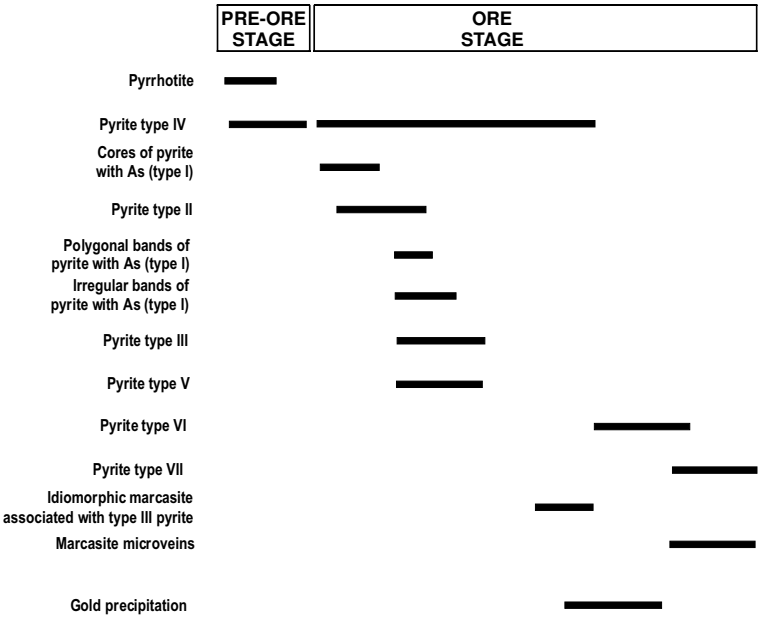


FIG. 14. Paragenetic sequence of the different types of Fe-sulphides showing their relationship with the gold at Palai-Islica mineralization.

contents. However, this correlation might be explained by either the entrance of cationic As and/or non-stoichiometric As (Fleet and Mumin, 1997). Although the presence of collomorphic textures does not necessarily imply colloidal origin (Roedder, 1968), colloidal precipitation is nonetheless an attractive hypothesis to explain the particular textural and chemical characteristics of the collomorphic pyrite overgrowths, since colloidal particles might be quite effective in trapping As ions. Colloidal particles with an As covering (negatively charged), could in turn act as 'traps' for cations. This mechanism could explain the relatively large amounts of Cu, Ag, Sb, Zn and Ni, as well as the Fe deficit found in the collomorphic pyrite overgrowths.

### *Type III pyrite-chalcopyrite-marcasite association*

The mineral association of type III pyrite-chalcopyrite-marcasite could be related to the formation of Au-Ag alloy horizons because of its location at the top of the horizons. The low $\delta^{34}S$ signature of these sulphides, different from the rest of the deposit (author data) could be caused by another kind of fluid implicated in the mixing processes, mentioned by Morales Ruano *et al.* (2000).

The high Ag and Cu contents of type III pyrite, and of As and Sb in marcasite are notable. We can infer from Fig. 9 two paths for the entry of Cu into pyrite: (1) below 0.10 at.% Cu (with which there is no concomitant increase in Ag). It is widely spread through the pyrite crystals (Fig. 3); (2) Above 0.10 at.% Cu, the increase in Cu is in a 1:1 relationship with Ag. These high concentrations of Cu and Ag not are due to the presence of microscopic inclusions as optical study shows, so they must be produced by (a) very abundant submicroscopic inclusions of chalcopyrite and/or Cu-Ag phases always intergrown with chalcopyrite, and (b) a true solid solution of Cu and Ag.

The entry of As in marcasite is the same as for type I pyrite, due to the 1:1 correlation between As and S. In addition, a small amount of Sb enters the marcasite when the concentration of As is >0.10 at.%. It seems that the maximum Sb occurs at ~0.20 at.% of As.

We explain the chalcopyrite disposition between marcasite and pyrite as the result of a diffusion process in which Cu migrates, to the limit between pyrite and marcasite. This process also liberates Ag to form Ag mineral inclusions (Ag suphides and sulphosalts).

### *Relationships between pyrite habit and gold crystals*

We have found a close relationship between the pyrite habit and the presence of gold crystals. Specifically, the gold is found on the mineralized levels containing type IV pyrite displaying a great variety of crystallographic habits (cubes and pentagonal dodecahedrons or octahedrons and pentagonal dodecahedrons). In contrast, barren zones occur where only the pentagonal dodecahedral morphology is developed.

Correlations between pyrite morphology and metal-enriched zones has also been described in other deposits (e.g. Sunagawa, 1957; Bush *et al.*, 1960; Amstutz, 1963). Pyrite morphology is determined by crystalline growth mechanisms (primarily screw dislocation and layer-by-layer), which are dependent on the temperature and degree of supersaturation of the fluid (Murowchick and Barnes, 1987). Pyrite deposition in the Au-mineralized zones in Palai-Islica may have been associated with a change in the degree of supersaturation of the mineralizing fluid, possibly due to mixing of fluids suggested by the fluid inclusion data reported by Morales Ruano *et al.* (2000).

### *Au and Ag contents in pyrite*

The Au contents obtained by EPMA for the different pyrite types are uniformly low (Tables 2 and 3). Selected high-acquisition-time analysis of different pyrite types (Table 4) also present low Au contents, never greater than the detection limit of 475 ppm, even in the As-rich pyrites which are considered to be potentially invisible-gold-bearing (e.g. Cook and Chryssoulis, 1990). These results, in addition to the abundance of visible gold grains, suggest that invisible gold may not be volumetrically significant in the overall deposit (Carrillo Rosúa *et al.*, 2002), as in other deposits where Au in pyrite reaches more than 1000 ppm (e.g. Mao, 1991; Fleet *et al.*, 1993; Asadi *et al.*, 1999; Simon *et al.*, 1999).

The relatively large values of Ag, found in the type III pyrite (up to 1.47 wt.%) and in the type VI collomorphic pyrite (up to 0.2 wt.%), are worthy of note. This Ag concentration is one of the highest found in pyrite to date (Larocque *et al.*, 1995, up to 1426 ppm; Griffin *et al.*, 1991, up to 625 ppm; Tompkins *et al.*, 1997, up to 200 ppm; Roberts, 1982, up to 300 ppm; Ashley *et al.*, 2000, up to 88 ppm). In our case, the supply of Ag by the pyrite to the deposit as a whole could be noteworthy, especially in the superficial zones

TABLE 4. Large-acquisition-time microprobe analyses for Au in different types of pyrite (wt.%).

| Pyrite type | S | Fe | As | Co | Ni | Total | Au (ppm) |
|---|---|---|---|---|---|---|---|
| I | 51.96 | 45.70 | 0.10 | 0.16 | 0.18 | 98.09 | 10 |
| I-II | 48.93 | 44.20 | 2.78 | 0.24 | 0.08 | 96.22 | 120 |
| I-II | 50.16 | 44.89 | 2.49 | 0.33 | 0.07 | 97.95 | 50 |
| I-II | 51.96 | 45.86 | 0.59 | 0.10 | 0.09 | 98.59 | 160 |
| II-I | 50.97 | 44.06 | 0.70 | 0.66 | 0.41 | 96.79 | 30 |
| II-I | 51.13 | 44.76 | 0.89 | 0.46 | 0.31 | 97.54 | 70 |
| IV | 51.59 | 45.31 | 0.02 | 0.07 | 0.00 | 97.00 | 120 |
| IV | 52.16 | 45.75 | 0.03 | 0.07 | 0.00 | 98.01 | 140 |
| IV | 52.38 | 46.08 | 0.01 | 0.06 | 0.00 | 98.53 | 0 |
| IV | 52.19 | 45.93 | 0.17 | 0.07 | 0.02 | 98.37 | 120 |
| VI-B | 48.88 | 42.68 | 4.86 | 0.06 | 0.00 | 96.48 | 30 |
| VI-B | 49.40 | 42.10 | 5.72 | 0.06 | 0.00 | 97.27 | 30 |
| VI-B | 47.70 | 41.04 | 5.42 | 0.05 | 0.00 | 94.21 | 140 |
| VI-B | 49.22 | 42.87 | 5.45 | 0.06 | 0.00 | 97.60 | 130 |
| VI-B | 49.51 | 42.23 | 5.55 | 0.06 | 0.00 | 97.34 | 60 |
| Minimum | 47.70 | 41.04 | 0.01 | 0.05 | 0.00 | 94.21 | 0 |
| Maximum | 52.38 | 46.08 | 5.72 | 0.66 | 0.41 | 98.59 | 160 |
| Average | 50.54 | 44.23 | 2.32 | 0.17 | 0.08 | 97.33 | 81 |
| St. dev. (1σ) | 1.51 | 1.65 | 2.41 | 0.18 | 0.13 | 1.13 | 54 |

of the deposit, where there are no other Ag-bearing phases apart from type VI pyrite.

### *Implications for the formation conditions of the presence of marcasite*

According to Murowchick and Barnes (1986) if marcasite crystallizes directly from a hydrothermal fluid, which is the case for the Palai-Islica deposit, then the pH must be <5. Therefore, low pH, at least, is expected at several points: large-scale silicification, hydrothermal alteration in the deepest part of the deposit, the formation of pyrite micro-geodes and the formation of idiomorphic marcasite (related to the Au-Ag alloy levels).

## Conclusions

(1) In this study we have noted the great usefulness of backscattered electron images obtained by SEM to determine heterogeneities in compositions in pyrites appearing homogeneous under reflected light. It is nevertheless necessary to use X-ray mapping with EPMA since SEM cannot detect anomalies of elements that do not have high atomic weights, commonly present in pyrites in hydrothermal deposits (Co and Ni). Therefore, EPMA is worthwhile, despite being less versatile and more time-consuming (~90 min to obtain values for four elements).

(2) Most of the pyrite formed directly from the hydrothermal fluid, although pyrrhotite and framboidal pyrite may also have acted, to a lesser extent, as precursors to pyrite during the first stages of crystallization.

(3) Among the trace elements in pyrite, As is the most abundant, with significant Co and Ni. These elements are distributed in bands and cores of medium- to coarse-grained pyrite crystals, indicating that they were incorporated in the pyrite structure during the early stages of pyrite crystallization. Arsenic and, to a lesser degree, Ni, Ag and Cu, can also be concentrated in the late stages of pyrite crystallization (as collomorphic pyrite).

It is probable that As enters the pyrite structure in two ways: (1) as a metastable solid solution (inverse correlation of As with S) with no significant entry of other elements, or (2) as a non-stoichiometric element by colloidal precipitation (inverse correlation of As *vs.* S and of As *vs.* Fe). The latter is associated with the entry of other trace elements, such as Cu, Sb, Ag and Ni. Cobalt and Ni substitute for Fe in the pyrite structure.

Marcasite also has significant amounts of As (with a crystallochemical behaviour similar to type I pyrite), and to a smaller extent of Sb. This

phase, together type III pyrite, may have undergone a diffusion process.

(4) The medium- to coarse-grained pyrite lacking trace elements (type IV) is the only host to Au-Ag alloys. These alloys, together with the native gold, are the main gold-bearing phases. The so-called invisible gold in the pyrite is of minor importance. However, the pyrite occasionally contains significant amounts of Ag in some textural varieties (e.g. types III and VI pyrite).

(5) Since the gold is closely associated with the pyrite, its extraction would necessarily involve large volumes of pyrite with high concentrations of heavy metals (As, Co and Ni), all highly contaminating. Given the proximity of the deposit to the Cabo de Gata Natural Park, the mining of this deposit would require special measures to minimize the environmental impact.

## Acknowledgements

The authors thank Serrata Resources S.A. for the help they have provided during this investigation. This research has also been supported by the projects No. PB-97-1211, BTE2001-3308 and RNM-0131 Research Group of the Junta de Andalucía. We thank Dr Peter Poltz (FELMI-ZFE, Graz University of Technology) for his help with FESEM study of pyrite and Prof. C. Laurin for correcting the English.

## References

Amstutz, G.C. (1963) Accessories on pyrite, pyrite zoning, and zoned pyrite. *Schweizerische Mineralogische und Petrographische Mittteilungen*, **33**, 111–122.

Arehart, G.B., Chyssoulis, S.L. and Kesler, S.E. (1993) Gold and arsenic in iron sulfides from sediment-hosted disseminated gold deposits: implications for depositional processes. *Economic Geology*, **88**, 171–185.

Arribas, A. and Tosdal, R. (1994) Isotopic composition of Pb in ore-deposits of the Betic Cordillera, Spain. Origin and relationship to other European deposits. *Economic Geology*, **89**, 1074–1093.

Arribas, A., Cunningham, C.G., Rytuba, J.J., Rye, R.O., Kelly, W.C., Podwysocki, M.H., McKee, E.H. and Tosdal, R.M. (1995) Geology, geochronology, fluid inclusions, and isotope geochemistry of the Rodalquilar gold alunite deposit, Spain. *Economic Geology*, **90**, 795–822.

Asadi, H.H., Voncken, J.H.L. and Hale, M. (1999) Invisible gold at Zarshuran, Iran. *Economic Geology*, **94**, 1367–1374.

Ashley, P.M., Creagh, C.J. and Ryan, C.G. (2000) Invisible gold in ore and minerals concentrates from the Hillgrove gold-antimony deposits, NSW, Australia. *Mineralium Deposita*, **35**, 285–301.

Benning, L.G., Wilkin, R.T. and Barnes, H.L. (2000) Reaction pathways in the Fe-S system below 100ºC. *Chemical Geology*, **167**, 25–51.

Boyle, R.W. (1979) The geochemistry of gold and its deposits. *Geological Survey of Canada Bulletin*, **280**.

Bush, J.B., Cook, D.R., Lovering, T.S. and Morris, H.T. (1960) The Chief Oxide-Buring area discoveries, East Tintic district, Utah; A case history – Part 1, U.S.G.S. studies and exploration. *Economic Geology*, **55**, 1116–1147.

Carrillo Rosúa, F.J., Morales Ruano, S. and Fenoll Hach-Alí, P. (2001*a*) Mineralogy and mineral chemistry of precious metals of the Cu-Au mineralisation at the Palai-Islica deposit, Almería, SE Spain. Pp. 715–718 in: *Mineral Deposits at the Begining of the 21st Century* (A. Piestrzyñski *et al.*, editors). Balkema, Lisse, The Netherlands.

Carrillo Rosúa, F.J., Morales Ruano, S. and Fenoll Hach-Alí, P. (2001*b*) Tipología de la pirita en el depósito epitermal de Palai-Islica (Carboneras, Almería). Implicaciones en la génesis del oro. *Boletín de la Sociedad Española de Mineralogía*, **24-A**, 151–152.

Carrillo Rosúa, F.J., Morales Ruano, S. and Fenoll Hach-Alí, P. (2002) The three generations of gold in the Palai-Islica epithermal deposit, Southeastern Spain. *The Canadian Mineralogist*, **40**, 1465–1481.

Clark, L.A. (1960) The Fe-As-S system: Phase relations and applications. *Economic Geology*, **55**, 1345–1381.

Cook, N.J. and Chryssoulis, S.L. (1990) Concentrations of 'invisible gold' in the common sulphides. *The Canadian Mineralogist*, **28**, 1–16.

Craig, J.R., Vokes, F.M. and Solberg, T.N. (1998) Pyrite: physical and chemical textures. *Mineralium Deposita*, **34**, 82–101.

Dewey, J.F. (1988) Extensional collapse of orogens. *Tectonics*, **7**, 1123–1140.

Fernández Soler, J.M. (1996) *El vulcanismo calco-alcalino en el Parque Natural de Cabo de Gata-Nijar (Almeria). Estudio volcanológico y petrológico*. PhD thesis, Universidad de Granada. Sociedad Almeriense Historia Natural, 295 pp.

Fleet, M.E. (1978) The pyrrhotite-marcasite transformation. *The Canadian Mineralogist*, **16**, 31–35.

Fleet, M.E. and Mumin, A.H. (1997) Gold-bearing arsenian pyrite and marcasite and arsenopyrite from Carlin Trend gold deposits and laboratory synthesis. *American Mineralogist*, **82**, 182–193.

Fleet, M.E., McLean, P.J. and Barbier, J. (1989) Oscillatory-zoned As-bearing pyrite from strata-bound and stratiform gold deposits: An indicator or

ore fluid evolution. Pp. 356–362 in: *The Geology of Gold Deposits: The Perspective in 1988* (R.R. Keays, W.R.H. Ramsay, and D.I. Groves, editors). Economic Geology Monograph, **6**. Economic Geology Publishing Company, El Paso, Texas.

Fleet, M.E., Chryssoulis, S.L., MacLean, P.J., Davidson, R. and Weisener C.G. (1993) Arsenian pyrite from gold deposits. Au and As distribution investigated by SIMS and EMP, and colour staining and surface oxidation by XPS and LIMS. *The Canadian Mineralogist*, **31**, 1–17.

García Dueñas, V., Balanya, J.C. and Martínez Martínez, J.M. (1992) Miocene extensional detachments in the outcropping basements of the northern Alboran Basin (Betics). *Geomarine Letters*, **12**, 88–95.

Griffin, W.L., Ashley, P.M., Ryan, S.G., Sie, S.H. and Suter, G.F. (1991) Pyrite geochemistry in the North Arm epithermal Ag-Au deposit, Queensland, Australia: A proton-microprobe study. *The Canadian Mineralogist*, **29**, 185–198.

Huston, D.L., Sie, S.H., Suter, G.F., Cooke, D.R. and Both, R.A. (1995) Trace elements in sulfide minerals from eastern Australian volcanic hosted massive sulfide deposits: Part I. Proton microprobe analyses of pyrite, chalcopyrite, sphalerite, and Part II. Selenium levels in pyrite: comparison with $\delta^{34}S$ values and implications for the source of sulfur in volcanogenic hydrothermal systems. *Economic Geology*, **90**, 1167–1196.

IGME (Instituto Geológico y Minero de España) (1974) *Mapa Geológico de España*. Escala 1:50,000. Hoja 1046 (24–42): Sorbas. Servicio de publicaciones Ministerio de Industria.

Kostov, I. and Minceva-Stefanova, J. (1981) *Sulphide Minerals. Crystal Chemistry, Paragenesis and Systematics*. Bulgarian Academy of Sciences, 212 pp.

Larocque, A.C.L., Jackman, J.A., Cabri, L.J. and Hodgson, C.J. (1995) Calibration of the ion microprobe for the determination of silver in pyrite and chalcopyrite from the Mobrun VMS deposit, Rouyn-Noranada, Quebec. *The Canadian Mineralogist*, **33**, 361–372.

López Ruiz, J. and Rodriguez Badiola, E. (1980) La región volcánica del sureste de España. *Estudios Geológicos*, **36**, 5–63.

Mao, S.E. (1991) Occurrence and distribution of invisible gold in a Carlin-type gold deposit in China. *American Mineralogist*, **76**, 1964–1972.

Morales Ruano, S. (1994) *Mineralogía, geoquímica y metalogenia de los yacimientos hidrotermales del SE de España*. PhD thesis, Universidad de Granada, Spain, 254 pp.

Morales Ruano, S., Carrillo Rosúa, F.J., Fenoll-Hach-Alí., P., de la Fuente Chacón, F. and Contreras López, E. (1999) The Au-Cu epithermal deposit at Palai-Islica deposit (Almeria, Southeastern Spain) Preliminary data. Pp. 59–62 in: *Mineral Deposits: Processes to Processing* (C.J. Stanley *et al*., editors). Balkema, Rotterdam, The Netherlands.

Morales Ruano, S., Carrillo Rosúa, F.J., Fenoll-Hach-Alí., P., de la Fuente Chacón, F. and Contreras López, E. (2000) Epithermal Cu-Au mineralisation in the Palai-Islica deposit, Almería, Southeastern Spain, fluid inclusion evidence of mixing of fluids as a guide to gold mineralisation. *The Canadian Mineralogist*, **38**, 553–566.

Murowchick, J.B. and Barnes, H.L. (1986) Marcasite precipitation from hydrothermal solutions. *Geochimica et Cosmochimica Acta*, **50**, 2615–2629.

Murowchick, J.B. and Barnes H.L. (1987) Effects of temperature and degree of supersaturation on pyrite morphology. *American Mineralogist*, **72**, 1241–1250.

Pouchou, J.L. and Pichoir, F. (1984) Un nouveau modèle de calcul pour la microanalyse quantitative per spectrométrie de rayons X. *La Reserche Aèrospatiale*, **3**, 167–192.

Ramdohr, P. (1980) *The Ore Minerals and their Intergrowths*. Pergamon Press, Oxford, UK, 1202 pp.

Roberts, F.I. (1982) Trace element chemistry of pyrite: a useful guide to the occurrence of sulphide base metal mineralisation. *Journal of Geochemical Exploration*, **17**, 49–62.

Roedder, E. (1968) The noncolloidal origin of 'collomorphic' textures in sphalerite ores. *Economic Geology*, **63**, 451–471.

Rösler, H.J. (1983) *Lehrbuch der Mineralogie*. VEB Deutscher Verlag für Grundstoffindustrie, Leipzig, Germany, 886 pp.

Rypley, E.M. and Chryssoulis S.L. (1994) Ion microprobe analysis of platinum-group elements in sulphide and arsenide minerals from the Babbitt Cu-Ni deposit, Duljth complex, Minnesota. *Economic Geology*, **89**, 201–210.

Savage, K.S., Tingle, T.N., O'Day, P.A., Waychunas, G.A. and Bird, D.K. (2000) Arsenic speciation in pyrite and secondary weathering phases, Mother Lode Gold District, Tuolumne County, California. *Applied Geochemistry*, **15**, 1219–1244.

Simon, G., Huang H., Penner-Hahn, J.E., Kesler, S.E. and Kao, L.H. (1999) Oxidation state of gold and arsenic in gold-bearing arsenian pyrite. *American Mineralogist*, **84**, 1071–1079.

Sunagawa, I. (1957) Variation in the crystal habit of pyrite. *Geological Survey of Japan Report*, **175**, 1–47.

Tompkins, L.A., Groves, D.I., Windrim, D.P., Jablonski, W. and Griffin, W.L. (1997) Petrology, mineral chemistry, and significance of Fe-sulphides from the metal dispersion halo surrounding the Cadjebut Zn-

Pb MTV deposit, Western Australia. *Applied Geochemistry*, **12**, 37–54.

Turner, S.P., Platt, J.P., George, R.M.M., Kelley, S.P., Pearson, D.G. and Nowell, G.M. (1999) Magmatism associated with orogenic collapse of the Betic-Alboran domain, SE Spain. *Journal of Petrology*, **40**, 1011–1036.

Wilkin, R.T. and Barnes, H.L. (1997) Formation processes of framboidal pyrite. *Geochimica et Cosmochimica Acta*, **61**, 323–339.

[*Manuscript received 25 April 2002: revised 16 June 2003*]